Multiple magma sources beneath the Okmok caldera as inferred from local earthquake tomography

By

Ekaterina Kasatkina (1), Ivan Koulakov *(1,2), Ronni Grapenthin (3), Pavel Izbekov (3), Jessica F. Larsen (3), Nassir Al Arifi (4), and Saleh Ismail Qaysi (4)

* Corresponding author. Email: KoulakovIY@ipgg.sbras.ru

1. Trofimuk Institute of Petroleum Geology and Geophysics SB RAS, Prospekt Koptyuga, 3, 630090, Novosibirsk, Russia, Kasatkinaev@ipgg.sbras.ru, KoulakovIY@ipgg.sbras.ru
2. Institute of the Earth's Crust SB RAS, Irkutsk, Russia.
3. Geophysical Institute, University of Alaska Fairbanks, rgrapenthin@alaska.edu, peizbekov@alaska.edu, jflarsen@alaska.edu.
4. King Saud University, Riyadh, Saudi Arabia, P.O. Box 2455, Riyadh 11451, Saudi Arabia, nalarifi@ksu.edu.sa, sqaysi@ksu.edu.sa

Submitted to Journal of Geophysical Research

April, 24, 2022

Kasatkina, E., Koulakov I., Grapenthin, R., Izbekov, P., Larsen, J.F., Al Alifi, N., and Qaysi, S.I. (2022). Multiple magma sources beneath the Okmok caldera as inferred from local earthquake tomography, *Journal of Geophysical Research, Solid Earth*.

Abstract

Okmok volcano located on the northeastern part of the Umnak Island is one of the most active volcanoes in the Aleutian Arc. It was initially built as a large shield volcano, but was strongly destroyed by two caldera-forming eruptions 12,000 and 2,040 years ago. The post-caldera eruptions occur mostly along the inner perimeter of the caldera from a series of distinct cones. Here, we perform seismic tomography to explore the deep sources of magmatic activity beneath Okmok. We use the local earthquake data of the Alaska Volcano Observatory (AVO) in the time period from 2003 to 2017 to build a model with the 3D distributions of the *P* and *S* wave velocities and *Vp/Vs* ratio. At depths of more than 10 km, we observe a vertically aligned anomaly of high *Vp/Vs* ratio representing a steady conduit likely responsible for the volcano evolution since its origin. Above this conduit, we reveal a large anomaly of high *Vp/Vs* ratio representing the main magma reservoir providing the material for all recent eruptions in the caldera. It appears to be connected with another large shallow reservoir located below the Cone A that was the source of most of Okmok's historical eruptions. The most recent eruption in 2008 took place right above the deep conduit. To reach the surface, the magma for this eruption passed through the shallow ductile zone, where it was saturated by silicic components. This interpretation is consistent with the petrology studies and modeling of ground deformations.

Plain Language Summary

Okmok is one of the most active volcanoes of the Aleutian Arc. Initially it was formed as an isometrical shield volcano, which was later destroyed by two caldera-forming eruptions. The post-caldera activity mostly occurred at several cones distributed along the inner perimeter of the caldera. The latest eruption with the explosivity index of VEI 4 took place in 2008. This eruption, which produced a new large cone Ahmanilix in the northeastern part of the caldera, was significantly different in composition and eruption style compared to other intra-caldera eruptions. We present a new seismic tomography model, which was constructed based on the arrival times of the *P* and *S* waves from local seismicity. Below 10 km depth, we observe an anomaly of high *Vp/Vs* ratio, which may represent a steady magma conduit that is responsible for the long-term formation of the entire Okmok volcanic complex. In the upper crust, the model reveals a series of separate local magma sources beneath volcanic centers where historical eruptions took place. The 2008 eruption was fed by a magma diapir that was initially formed in the deep conduit and then slowly ascended through a ductile layer at depths from 6 to 2 km.

Key points:

- The new crustal model beneath the Okmok Caldera with the 3D distributions of Vp, Vs and Vp/Vs ratio reveals the geometry of magma sources
- Below 10 km depth, an anomaly of high Vp/Vs ratio indicates the location of the main magma conduit that fed the long-term formation of Okmok
- At shallow depths, seismic anomalies reveal several magma sources that fed eruptions along the inner perimeter of the caldera

Key words: Seismic tomography, Okmok caldera, Aleutian Arc, magma sources, volcanic eruption

Introduction

Okmok is one of the most active volcanoes of the Aleutian Arc. Initially, it was founded as a large circular shield volcano with a diameter of ~30 km that occupies the northeastern half of the dumbbell-shaped Umnak Island. According to the K-Ar dating, the formation of this volcano began approximately 1.7-2.1 Ma (Birgham and Stone, 1972), which indicates the existence of a long-term steady magma conduit existing for millions years. The central part of this volcano was destroyed by at least two ignimbrite-forming eruptions 12,000 and 2,050 years ago (Larsen et al., 2007) that created two overlapped well-exposed circular calderas with the total size of ~10 km (Figure 1). The amount of material in dense rock equivalent for these two eruptions was estimated as 30 km^3 and 15 km^3, respectively (Larsen et al., 2007). These eruptions had an important impact on the climate that was felt globally. There is evidence that the latter eruption affected people in Europe and caused serious historical perturbations (McConnel et al., 2020). Untypically for caldera-forming eruptions, the products of these two eruptions contained very little amount of rhyolite and dacite magmas, which were ejected at the initial stages, but then were replaced by a larger amount of andesite and basaltic andesite (Larsen et al. 2007).

The post-caldera eruption activity mostly occurred along the inner perimeter of the caldera through a series of vents some of which created well-expressed cinder and tuff cones indicated by letters from A to H (Figure 1). The compositions of these eruptions were mainly basaltic. The oldest flows were composed of pillow lavas, which indicated that the caldera was initially filled by a deep lake (Larsen et al. 2007). Nowadays, in the caldera, there are several

shallow lakes that are abruptly changing their configurations during eruptions. Besides the intra-caldera eruptions, there were several flank eruptions forming a few outer cones of which the largest are Tulik and Jag Peaks.

At least 17 historical explosive and effusive eruptions have been recorded on Okmok since the beginning of the nineteen century (Larsen et al., 2015). The majority of these eruptions occurred from the cone A in the southwestern part of the caldera. In the twentieth century, the well-documented eruptions with basaltic-andesite lava flows and moderate ash falls occurred in 1945, 1958 and 1997 exclusively from the vent A (e.g., Miller et al., 1998, Larsen et al., 2015).

The latest eruption with the high explosivity index of VEI 4 took place in July-August 2008 and it appeared to be among the strongest historical eruptions of Okmok. It occurred in the northeastern part of the caldera close to the Cone D and produced a new large cone called Ahmanilix. This eruption was classified as explosive phreatomagmatic eruption with a large amount of steam, ash and tephra ejected. According to the geochemical analyses by Larsen et al. (2013), the eruption products in this part of caldera are distinctively different from those in the southwestern part around the A cone; namely they have higher SiO_2 content. A specific feature of the 2008 eruption is that it almost did not produce any lava flows (Larsen et al., 2015). Unlike the previous instrumentally recorded events of volcanic activity of Okmok, the eruption of 2008 was not preceded by any significant seismic precursors. For ten days prior to the eruption, only 11 locatable earthquakes were recorded. An active seismogenic process started only five hours before the eruption onset (Larsen et al., 2009).

Okmok's dynamic and near-continuous deformation during and in between eruptions made it the subject of many studies using GPS, InSAR, or both to constrain its subsurface magma system structure and its evolution. The 1997 and 2008 eruptions caused meter-scale deflation of the caldera center (e.g., Mann et al, 2002; Freymueller and Kaufmann, 2010), while inter-eruptive deformation is characterized by discrete inflation pulses modulated onto steady background inflation of several centimeters per year (e.g., Qu et al., 2015; Xue et al, 2020) . Inversions of InSAR data (e.g., Lu et al., 2000, Mann et al., 2002; Qu et al., 2015; Lu & Dzurisin, 2014), GPS data (e.g., Fournier et al., 2009; Freymueller and Kaufmann, 2010) or joint inversions of both (e.g., Biggs et al., 2010; Xue et al., 2020) generally yield a spherical magma reservoir near the center of the caldera between 2-5 km depth, with most results placing the source between 2-3.5 km. Xue et al. (2020) suggested that in addition to this spherical source a shallow sill at about 0.9 km is necessary to explain the post-2008 geodetic observations. They also count five inflation pulses since the 2008 eruption that emerge rapidly and slow down

following an exponential decay. Walwer et al. (2019) explained the origin of these short-term inflation pulses by hydraulic interaction between two shallow magma chambers.

Another group of studies examined structure and dynamics of magma sources beneath Okmok based on the analysis of seismic data, which were continuously recorded by a network of permanent telemetric seismic stations operated since 2003 (Dixon et al., 2017). The temporary and spatial distributions of volcano-tectonic events during the eruption in 2008 were investigated by Johnson et al. (2010), who also provided estimates for seismic anisotropy based on the shear wave splitting technique. Moment tensors of these events were determined by Pesicek et al. (2012). Haney et al. (2010) investigated the very long-period seismicity, which was the indicator of magma dynamics in the conduit and therefore was considered as one of the eruption precursors.

In the context of this research, it is important to mention the previous seismic tomography studies of the Okmok area. The ambient noise tomography method was used by Masterlark et al. (2010) to build the 3D distribution of the *S*-wave velocity down to 7 km depth. They identified a low-velocity anomaly right below the caldera, which was interpreted as deposits of non-consolidated rocks accumulated after the latest caldera-forming eruptions. Another anomaly was observed at depths of 3-5 km below the caldera and was associated with the presence of the shallow magma reservoir. Later this model was used together with data on ground deformations to validate the numerical model of magma source dynamics (Masterlark et al., 2012). However, it should be noted that this model was constructed on the basis of only 12 stations, of which 9 were equipped by single-component short period sensors (1 Hz). This network provided a limited number of inter-station paths and could not enable high lateral resolution of the resulting velocity distribution, especially at large depths.

Another tomography model by Ohlendorf et al. (2014) was constructed based on the local earthquake tomography using generally the same principle and data type as in our work. They reported both the models of the *P* and *S*-wave velocities, as well as the distribution of the *P*-wave attenuation; however, the authors admitted that their *S*-wave model was based on too sparse data coverage and therefore was not robust. Similarly as in the model by Masterlark et al. (2010), the body wave tomography revealed low *P*-wave velocity beneath the caldera; however, the *S*-wave velocity was unexpectedly high in the same locations. Note also, that in this model, the resolution suffered from too large grid spacing making the results strongly grid-dependent. Furthermore, the authors did not present the distribution of the *Vp/Vs* ratio, which appeared to be the key parameter to identify magma sources beneath active volcanoes.

In this study, we construct a new seismic velocity model based on a considerably enlarged dataset and using another tomography code LOTOS (Koulakov, 2009), which previously demonstrated its efficiency for studying different volcanic systems in the world (Kasatkina et al., 2014, Koulakov et al., 2013, Bushenkova et al., 2019). Here, we will pay special attention to showing the distributions of the *Vp/Vs* ratio, which is presumed the most sensitive seismic attribute to the presence of partially molten and fluid saturated magma. In this study, we will present several synthetic tests showing the resolution limitations of our model. Therefore we claim that the results presented in this work give important new information on the magma system structure beneath Okmok compared to the previous studies and therefore brings an important contribution to understanding the processes leading to initiation of eruptions.

Data and algorithms

In this work, we use the catalog data from 2003 to 2017, which includes the arrival times of the *P* and *S* waves from local seismicity recorded by 13 permanent telemetric stations located around Okmok and operated by the Alaska Volcano Observatory (AVO) (Dixon et al., 2017). Of these stations, four are equipped with the broadband seismometers Guralp CMG-6T; the remaining nine are based on the short-period (1Hz) single-component sensors L-4 (Figure 2). However, for determination of arrival times from the local seismicity, the frequency ranges of the both types of seismometers are equally suitable. The initial catalog includes 4,174 events and the corresponding arrival times of 19,249 *P* and 14,278 *S* waves (on average 8.03 picks per event). To select data for the tomography inversion, we applied several criteria: (1) the number of picks per event should be equal or larger 8; (2) the time residuals after the source location in the starting 1D model should be smaller than 0.5 s; (3) the horizontal distance from an event to the nearest station should be less than 20 km. After the selection, the final dataset used for tomography included 2869 events with the corresponding 17,040 *P*- and 12,145 *S*-picks (on average 10.17 picks per event). The distributions of the events and seismic stations are shown in map view and in vertical projections in Figure 2. Further information on the event distributions after locations in the final 3D velocity model will be presented in cross-sections with the main tomography results.

These data were processed using the passive-source tomography algorithm LOTOS (Koulakov, 2009). As the input, the algorithm uses the arrival times of the *P* and *S* waves and it starts with the absolute locations of sources using the grid-search method and a simplified algorithm for travel time calculations along straight lines. Then the relocation of the sources is performed in an iteratively updated 3D velocity model with the use of a more sophisticated ray tracing algorithm based on a bending technique (Um and Thurber 1987).

The velocity model is parameterized with a set of nodes distributed in the 3D space. In map view, the nodes are installed regularly with a spacing of 1 km. In the vertical direction, the spacing is inversely dependent on the ray coverage, but should not be smaller than 0.5 km. In areas without rays, no nodes are installed. To reduce the effect of parameterization on the results, we performed the inversions in four grids with different basic orientations along the azimuths of 0, 22, 45 and 66 degrees, and then averaged the results.

The inversion of the matrix was performed simultaneously for the 3D *P* and *S* wave velocity anomalies (*dVp* and *dVs*) and source relocation parameters (coordinate shifts, *dx*, *dy*, *dz*, and origin time correction, *dt*). The inversion was performed using the Least Square algorithm with QR factorization (LSQR) (Page and Saunders, 1982; Nolet, 1987).To regularize the stability of the resulting velocity models, we used the amplitude damping and flattening that controlled the difference between all pairs of neighboring nodes. In our case, the values of the amplitude damping for the *P* and *S*-wave models were 0.5 and 1, respectively; the corresponding flattening coefficients were 0.7 and 1.5. These regularization parameters were identified based on the results of synthetic modeling, which will be presented below.

The iterative cycle included the steps of source locations in the updated 3D velocity model, matrix calculation, simultaneous inversions for four different grids and calculation of the new averaged 3D model. In total, we performed five iteration cycles, which was an appropriate compromise between the model stability and calculation speed. Note also that the tomography inversion provides the 3D distributions of the *P* and *S* wave velocity anomalies. The distribution of the *Vp/Vs* ratio is calculated by simple division of the resulting absolute *Vp* and *Vs*. The adequacy of this approach was tested by a series of synthetic tests, which will be presented in the next section.

Synthetic tests

Before presenting the main velocity models, we show the results of several synthetic tests demonstrating resolution limitations of the tomography results. We perform synthetic modeling to simulate the conditions of the experimental data processing as closely as possible. The synthetic travel times are calculated for the same source-receiver pairs, as in the experimental dataset, in the predefined 3D synthetic velocity model with the use of the bending ray tracing algorithms. The travel times are then perturbed by random noise with average deviations in the L1 norm equal to 0.03 s and 0.05 s for the *P* and *S* wave data, respectively. Then we “forget” any information about source coordinates and origin times and start the recovery using the same workflow as in the case of experimental data inversion, including the initial step of absolute

source locations. All the controlling parameters in the synthetic modeling remain the same as in the case of computing the main model.

Here, we separately analyze the horizontal and vertical resolution based on the same sections as used for presenting the main results. In the first test presented in Figure 3, we define the horizontal checkerboard model with alternated positive and negative anomalies of ±8% having the size of 5 km and separated by 1 km intervals. In the vertical direction, the anomalies remain unchanged at all depths. In the resulting horizontal sections in Figure 3, we can see that the anomalies are correctly recovered at all depths down to at least 7 km, although, in the deeper sections, the amplitudes of anomalies become weaker, which is explained by considerably smaller amounts of data.

In the next series of tests, we explore the vertical resolution of the models, which is usually poorer than the horizontal resolution due to the trade-off between velocity and source parameters (especially of focal depths). In Figure 4, we present three synthetic models separately defined along three vertical sections used for presenting the main results. Along the sections, we defined alternated anomalies with the amplitudes of ±8% having the sizes of 5 by 6 km. In the horizontal direction, they are separated by a 1 km interval. In the vertical direction, the interval is 2 km. The change of the anomaly sign occurs at the depth internals of 2-4 km and 10-12 km. In the resulting images, we can see that we can robustly resolve the upper two layers of anomalies, whereas the third layer below 12 km depth appears not to be recovered.

To further assess the capacity of our algorithm to resolve the deep structures we performed another series of tests presented in Figure 5, in which the anomalies are defined in a single layer located below 8 km depth. We see that most of the anomalies are recovered in the correct locations, which shows that such kinds of structures appear to be trustworthy.

To further assess the reliability of some structures inferred from the main results and used for interpretation, we have produced a series of tests with realistic anomalies that are presented in Figure 6. In this test, several patterns are defined along vertical section 1 by a series of closed polygons, in which we set some values of the *P* and *S* wave velocity anomalies (the values in percent are indicated in Figure 6 by numbers inside each pattern). Here, we consider two models with and without the deep conduit beneath the location of the 2008 eruption. In the recovery results (lower row in Figure 6), we can see that in Model 2 (without conduit), there is some downward smearing of the shallower anomalies, which can be misinterpreted as downgoing roots of this structure. However, this case is distinguishable from the result of the recovery of Model 1, in which we defined the deep conduit. These tests demonstrate that we should be

prudent when interpreting the structures below 10 km depth. Another structure, which is examined in this test is an anomaly located at the left end of the profile corresponding to the high-seismicity zone beneath the isthmus connecting two parts of the island. This area is located outside the network distribution, therefore, the reliability of the derived structures is questionable. In these tests, we defined a large anomaly in a broad range of depths with highly contrasted deviation of the Vp/Vs ratio. In the recovery result, we see that this anomaly is restored with much lower amplitude and at smaller depths. This test shows that we should be careful when considering numerical values of this structure and should only interpret it qualitatively.

It is important that in all tests, we present the distributions of the *Vp/Vs* ratio calculated by the division of the recovered absolute values of *Vp* and *Vs* and show fair recovery of the main structures. These examples show the adequacy of this approach.

The synthetic tests allow also for accessing the accuracy of source parameter determinations. In Figure 7, we present an example of mislocations of sources in the starting 1D model and in the final 3D velocity distributions in the recovered velocity model. This example corresponds to the case of the synthetic Model 1 with realistic anomalies presented in Figure 6. The black points depict the current hypocenter solutions, whereas the red bars direct to the true source locations. It can be seen that in the starting model, the mean error of source locations is 1.35 km, while in the final model, it is reduced to 1.05 km. The largest errors are observed in the southwestern part of the study area located outside the station network, which remain considerable after completing the iterative inversion procedure. At the same time, for areas inside the network, we can visually observe a notable improvement of the source locations during tomography inversions. The similar error range is expected in the case of the experimental data inversion.

Seismic tomography results

The main resulting distributions of the anomalies of *Vp* and *Vs*, as well as the *Vp/Vs* ratio are shown in a series of horizontal and vertical sections in Figures 8 and 9. All these results were calculated after five inversion cycles. During the iterative inversion procedure, the *P*-wave residual deviations in the L1 norm were reduced from 0.1455 s to 0.1084 s (25.51%), and those of the *S*-wave reduced from 0.1968 s to 0.1381 s (29.79%). The detailed interpretation of the resulting models will be presented in the next section. Here we only describe the most important structures obtained from seismic tomography.

As we can see in the horizontal section at a 0 level in Figure 8, in the shallowest part of the model, we observe prominent negative anomalies inside the caldera, which likely indicate non-consolidated deposits of volcaniclastic rocks. The *P*-wave velocity anomalies appear to be stronger and in some places exceed 20%. The stronger *P*-wave anomaly may be indicative for the porous structure of the material, which behaves as a sponge and has low bulk elastic modulus (Takei, 2002). In this case, the *Vp/Vs* shows strongly negative anomaly, which is quite typical for caldera-filling rocks (see, for example, a similar feature in the Semisopochnoi Island in the tomography model by Yaroshenko et al., 2022). In the vertical section (Figure 9), we can see that this anomaly of low *Vp/Vs* ratio is rather thin and hardly reaches 1 km. In the shallowest section, the only place within the caldera, where we observe a local anomaly of high *Vp/Vs* ratio, coincides with the cone A in the southeastern part of the caldera, which can be explained by the presence of the magma conduit close to the surface. Another low-velocity anomaly in the uppermost layer is associated with Mt. Tulik, which is a large cinder cone located outside the caldera, having similar mechanical properties as deposits in caldera.

At the depth of 4 km, the distributions of *dVp*, *dVs* and *Vp/Vs* ratio inside the caldera look considerably different compared to the upper section. The low *S*-wave anomaly almost perfectly coincides with the caldera contour, whereas the distribution of the *P*-wave velocity anomalies is more heterogeneous. Below the cones A and D, we observe locally high *P*-wave velocity patterns (indicated by "1" and "2"), which give the inverse correlation of *dVp* and *dVs* and high values of *Vp/Vs* ratio. Such a relationship is a clear attribute of the presence of the magma with some content of partial melts and fluid saturation, which is normally observed in tomography models for most active volcanoes (Kasatkina et al., 2014, Bushenkova et al., 2019; Koulakov et al., 2013).

In the vertical sections 1 and 2 (Figure 9), we can see that the upper level of the high-*Vp/Vs* anomaly "1" beneath the cone A is located at a depth of less than 500 m, and the bottom side is at ~5 km b.s.l. The lateral size of this anomaly is approximately 3 km. Beneath the Ahmanilix vent, newly opened during the 2008 eruption, in Sections 1 and 3, we see that the upper limit of the high *Vp/Vs* anomaly "2" is located at the depth of 2 km below surface. The lower limit of this anomaly is not clearly determined in our model: it rather looks as a chain of several structures aligned vertically. The upper anomaly "2" is identified at depths of 2 - 5 km, and the second one indicated by "3" is located at 6 to 10 km depth. Below, we observe a vertically oriented anomaly "4", which may represent a deep magma conduit. Based on the two synthetic models with realistic structures presented in Figure 7, despite some obvious vertical

298 smearing in the lower part of our model, we can distinguish such a conduit-related anomaly;
299 though, we should be careful about its numerical parameters.

300 The results in deep sections at 7 and 10 km depth look generally similar. The most
301 prominent feature is an anomaly of high *Vp/Vs* ratio indicated by "3" and "4", which is located
302 beneath the caldera and slightly shifted to its northwestern part, where the 2008 occurred. This
303 anomaly, which likely represents the deeper magma reservoir, is also marked by clustered
304 seismicity.

305 There are two other interesting seismic structures located outside the caldera. As we can
306 see in both horizontal and vertical sections, in the southwest corner of our study area, at the
307 isthmus between two parts of the island, a zone of high seismicity appears to be associated with
308 high *Vp*, low *Vs* and high *Vp/Vs* ratio. In vertical section 1, this anomaly indicated by "6" is
309 observed down to ~10 km depth. However, as was shown in the synthetic test with realistic
310 anomalies in Figure 7, in this part of the area, the available data do not enable high-quality
311 recovery, and we can only interpret it qualitatively. In horizontal sections, we see that this zone
312 seems to be connected with the caldera-related anomaly by elongated low-velocity anomalies.

313 Another zone of elevated seismicity is located in the offshore area, at the southern border
314 of the study area (indicated by "7"). This zone is located outside the station network, therefore
315 we cannot enable sufficient resolution for velocity recovery in this area. However, in the
316 horizontal sections, we see some elongated low-velocity anomalies that connect this zone with
317 caldera.

318 We can compare our results with the previous seismic tomography studies of Okmok.
319 Some of the images in the study by Ohlendorf et al. (2014), which were based on the generally
320 the same technique and data sources as in this work, appear to be consistent with our results. A
321 prominent low-velocity anomaly of the *P*-velocity inside the caldera determined by them seems
322 to be similar to our results, especially to the anomalies of the *S*-wave velocity. Similar
323 correlation is observed between their distribution of the *P*-wave attenuation and our *S*-wave
324 velocity model. However, in the *S*-wave velocity model, Ohlendorf et al. (2014) revealed a
325 prominent high-velocity velocity anomaly beneath the caldera, which appeared to be inversely
326 correlated with our result. Furthermore, they did not resolve several important features, such as
327 local high *Vp* anomalies at 4 km depth beneath the eruption centers of 1997 and 2008, as
328 apparent in our model, probably because of insufficient resolution and too sparse grid spacing.
329 At the same time, our *S*-wave velocity distribution fairly well correlates with the model by
330 Masterlark et al. (2010) constructed with the use of ambient noise tomography. In that study, the

low-velocity anomaly of *Vs* is observed beneath the caldera down to 7 km depth; for the deeper sections, they did not have a sufficient resolution.

Discussions

Seismic tomography is especially beneficial for identifying the properties of the magma plumbing system beneath active volcanoes, when several seismic attributes, such as *Vp*, *Vs* and *Vp/Vs* ratio can be determined. Based on the experience of previous seismic tomography studies (Koulakov et al., 2013, 2020, 2021; Koulakov, 2022) and the existing experimental results (Takei, 2002), we can single-out several regularities that can be useful to interpret the model obtained in this work. The *P*-wave velocity is primarily sensitive to the composition, whereas the variation of the *S*-wave velocity is mostly controlled by the presence of a liquid phase. The coexistence of higher *P*- and lower *S*-wave velocity, and the corresponding very high values of *Vp/Vs* ratio is a rather typical feature observed beneath many active volcanoes and interpreted as magma reservoirs or conduits (Bushenkova et al., 2019, Koulakov et al., 2013, 2020, 2021). Indeed, the intruded magma has a different composition compared to the host crustal rocks, which determines the higher *Vp*. On the other hand, the active magma sources contain some partial melts and dissolved volatiles that reduce the *S*-wave velocity. This feature provides a very high and contrasted *Vp/Vs* ratio, which is used to determine the geometry of the magma reservoirs and conduits.

It should also be noted that the *P* and *S* wave velocities, when considered separately, in many cases cannot provide unambiguous interpretation. For example, the high *Vp* can be associated with both highly solidified rigid bodies and fresh magma intrusions. The low *S*-wave anomalies can appear to be similar in cases of soft sediments and partially molten magma reservoirs. Thus, when only one of these parameters is available, misinterpretations are possible. The interpretation becomes less ambiguous, when the *Vp* and *Vs* are jointly considered. In particular, the *Vp/Vs* ratio gives clearer images of magma-associated structures, than *Vp* and *Vs* alone and it allows distinguishing the cases mentioned above. For example, considering only *Vs* in Masterlark et al. (2010) does not allow distinguishing between the low-velocity soft rock deposits and underlying magma sources. However, we see that the *Vp/Vs* ratio presented in our study successfully solves this problem and clearly differentiates between the low-*Vp/Vs* in sediments and the very high *Vp/Vs* ratio in the magma reservoir. Similar differentiation was observed in the area between Avacha and Koryaksky volcanoes (Bushenkova et al., 2019),

363 Akutan (Koulakov et al., 2021) and in many other places. For Okmok, the *Vp/Vs* ratio
364 demonstrates a very shallow location of the magma source beneath the cone A.

365 Based on the distribution of the *Vp/Vs* ratio in Figures 8 and 9, we can single out several
366 prominent anomalies that might be associated with magma sources. Our schematic interpretation
367 of these structures is presented in Figure 10. Below the cone A, at the intersection of sections 1
368 and 2 (Figure 9), we observe a contrasted anomaly "1" with the *Vp/Vs* exceeding 2. According to
369 our model, the upper limit of this anomaly is located at a depth of a few hundred meters and it
370 extends down to ~6 km. We interpret this anomaly as a magma reservoir that fed the multiple
371 eruptions of crater A that occurred in the historical times.

372 Below the cone D and the Ahmanilix vent formed during the 2008 eruption at
373 intersection of sections 1 and 3 (Figures 9 and 10), we observe a chain of the vertically oriented
374 anomalies of high *Vp/Vs* ratio. The deep part indicated by "4" represents a steady magma conduit
375 that is likely responsible for forming the Okmok volcano during the entire history of its
376 evolution. Its location roughly corresponds to the summit of the ancestral shield volcano that was
377 being formed here for more than a million of years, and the conduit is thought to have been
378 active for the same time span.

379 It appears to be paradoxical that the major recent activity in Okmok occured along the
380 perimeter of the caldera and not in the center, just above the conduit, where the strongest seismic
381 velocity anomalies are observed. Indeed, most of the historical eruptions, including one in 1997,
382 took place in cone A, which is laterally shifted to ~5-7 km from the conduit center. Similar shift
383 is observed for the 1817 eruption that occurred in the cone B in the northern part of the caldera.
384 The cones F, E, G, H are also located away from the conduit's projection to the surface. The
385 cones D and Ahmanilix were the only eruption centers, which appeared to be directly connected
386 with the conduit, but they were the result of monogenic episodes and had not a regular eruption
387 activity, like in the A cone. Similar offsets between magma reservoir and eruptive site exist at
388 other calderas. A notable example is Grimsvotn in Iceland, with a stable magma reservoir at the
389 northern caldera edge, yet the recent eruptions occurred at the southern caldera rim (e.g.,
390 Hreinsdottir et al., 2014).

391 We explain this paradox by the existence of a mechanical barrier under the central part of
392 the caldera that prevents magma ascending upward and coerces it to find other paths to the
393 periphery of the caldera. The long-term thermal effect from the conduit led to forming a ductile
394 layer with some content of partial melts. Based on the obtained distribution of the *Vp/Vs* ratio,
395 we propose that this layer corresponds to the anomaly "2" located at depths from 2 to 5 km,

perhaps to shallower depths as suggested by the recently proposed very shallow sill-like sources (Xue et al., 2020).

This ductile zone is underlain and likely well connected (Figure 9) to another anomaly of high Vp/Vs ratio indicated by "3". Together this shallow system may represent the major magma reservoir feeding the ongoing eruptions at Okmok. This is consistent with the magma source depth estimates obtained from ground deformation modeling, placing magma source regions in the 2-6 km range. This depth range may indicate that this part of the system is over time active at different depths, or the geodetic data cannot resolve simultaneous activity of both sources unless they are sufficiently separated. This is perhaps due to the limited aperture afforded to geodetic observations by the small radius of the main land mass.

The ductile medium in zone "2" may serve as a barrier for the magma to ascend directly to the surface. Soft rheology does not allow magma to create fractures, and it can only ascend in the form of diapirs due to buoyancy, which enables much slower movement than migration through a brittle medium (e.g., Sigmundsson et al., 2021). That is why, to escape from reservoir "3", for magma, it is easier to form some lateral conduits in colder brittle areas where migration can be conducted by hydraulic fracturing. In Figure 10, based on the distribution of the *Vp/Vs* ratio, we identify that such a conduit takes place between the anomalies "3" and "1" that delivers the magmatic material to the reservoir below the cone A. Such a transportation of magma between the reservoirs "3" and "1" likely occurred continuously during the recent epoch, when the regular historical eruptions occurred in the cone A. This has directly provided mafic material to the reservoir "1" from the deep conduit without significant changes at intermediate levels, which is consistent with available information on dominantly basaltic compositions of the eruption products from the Cone A (Larsen et al., 2013).

There might be a similar lateral magma conduit toward the anomaly "5" below the northern border of the caldera, which likely represented another magma reservoir that was responsible for the eruption of in 1817. Its upper limit is observed at ~4 km depth. As there is no activity in this part of the caldera for more than 200 years, any traces of shallow conduits bringing magma from the reservoir "5" to the surface were healed, and nowadays they are not visible in the tomography model.

The vertical ascents of magma that caused the formations of cones D and Ahmanilix are rather exceptional cases, which occurred only two times during the recent activity of Okmok. In these cases, the magma was able to pass through the ductile zone "2" and to reach the surface. This way of magma ascending is supported by the fact that no increase of seismicity was

observed before the 2008 eruption (Larsen et al., 2009; 2015). The seismic activity started only five hours prior to the eruption onset, and it likely represented the moment when magma came out from the ductile layer and reached the uppermost brittle cover. In this scenario, the magmas of the 2008 eruption should be contaminated by the rock components existing in zone "2". This is generally consistent with the concept of Larsen et al. (2013) who hypothesized that the 2008 eruption in the northeastern part of the caldera was fed by basaltic magma that initially arrived from a deep reservoir and then was intersected with a more evolved basalt-andesitic magma in shallower layers. This provided a broader range of compositions in different vents of the 2008 eruption compared to those of the 1997 eruption in the cone A.

In the southwestern corner of our study area near the isthmus separating two parts of the Umnak Island, there is an area of high geothermal activity called the Hot Springs Cove. Although it is located outside the seismic station network, a large number of seismic events was recorded in this zone. For seismic tomography, we cannot guarantee high resolution for the structures sitting there. As shown by the synthetic test with realistic anomalies, in this zone, we can only recover general background velocities. Here, we obtain higher *P* and lower *S* wave velocities. In the context of known geothermal activity, it is natural to propose that the low *dVs* are associated with high fluid saturation, which can reach significant depths. Based on the existing data, we can speculate that the observed seismicity at depths down to 8-10 km might be caused by upward migration of deep fluids, as the meteoric fluids cannot reach such depths. However, this hypothesis should be verified or disproved by geochemical examination of the hydrothermal sources. The adjacent area of high geothermal activity Geyser Bight was investigated by Nye et al. (1990) with the aim to explore the geothermal activity. In their report, they claimed that hydrothermal activity in this area was mostly driven by circulation of meteoric waters. However the ratio of 3He/4He=7.4 in emanating gas may provide evidence for a magmatic influence on the hydrothermal system. A similar effect of the deep processes on the hydrothermal processes may take place in the area of Hot Spring Cove.

It is interesting that in maps of the *P* and *S* wave velocity anomalies at 4 and 7 km, the area of the Hot Springs Cove is connected with the caldera by an elongated low velocity anomaly. It can be proposed that this structure represents a hidden tectonic fault that serves as a weakened zone facilitating migration of magma and fluids. Associations of such fault-related linear seismic velocity anomalies with volcanic and geothermal centers is a rather typical feature observed in several volcanic areas, such as Tolbachik in Kamchatka (Koulakov et al., 2017) and Toba Caldera in Sumatra (Koulakov et al., 2016). If there is a tectonic fault, the seismicity

beneath this zone can be of tectonic nature. However, the ruptures might be facilitated by the presence of deeply migrating fluids.

Conclusions

Here, we revisit the local earthquake data for the Okmok volcano provided by the Alaska Volcano Observatory to build a new seismic tomography model. Owing to implementing the LOTOS tomography algorithm with adapting parameterization and using a larger dataset compared to the previous study by Ohlendorf et al. (2014), we have obtained higher resolution for the resulting distributions of the *P* and *S* wave velocities and the *Vp/Vs* ratio. In the derived models we can identify some important features that were not seen before and that provide important insight on the geometry of magma sources beneath Okmok. A number of synthetic tests have demonstrated the resolution limitations for the recovered models and proven the reliability of the main structures used for the interpretation. To reveal the geometry of the magma sources, we mostly use the distribution of the *Vp/Vs* ratio, which appears to be a sensitive attribute for the presence of magma having different composition and containing partial melts and dissolved fluids.

Based on the retrieved seismic model, we conclude that the steady magma conduit, which is responsible for forming the entire Okmok volcanic complex, is located beneath the northeastern part of the caldera. At depths of 6-10 km, this conduit is headed by the main reservoir, which is thought to be the main magma source for all volcanic vents along the inner perimeter of the Okmok caldera.

We speculate that for the magma from the deep conduit, it is difficult to ascend vertically because of the presence of a ductile layer at the depth of 2-5 km that serves as a natural barrier for ascending magma. In the post-caldera time, only in two cases, magma could pass this layer and reach the surface. In the first case, it caused forming the monogenic cone D. The second eruption occurred in 2008 and resulted in forming the new cone Ahmanilix. In this sense, the vertical transport of magma directly from the deep conduit appears to be exceptional for Okmok.

In most cases, magma escapes from the central reservoirs toward the periphery of the caldera and creates local reservoirs beneath active vents. In historical times, the most active vent, where the majority of the recorded eruptions of Okmok occurred, corresponds to the cone A in the southwestern part of caldera. Below this location, we observe a large anomaly with the upper boundary located at the depth of a few hundred meters and the bottom at ~5 km depth, which

494 represents the magma reservoir that feeds all these eruptions. In our tomography model, we see
495 that this anomaly is connected with the central magma reservoir, which provides for continuous
496 infill of the storage below the crater A by fresh magma with mafic composition. Another
497 periphery reservoir and a conduit can be detected below the vent of the 1817 eruption; however,
498 it appears to be less clear, as it might have been dissipated during more than 200 years of
499 quiescence.

500 Our result shows that the magma reservoir beneath the cone A is located very close to the
501 surface, possibly at a few hundred meters depth. This finding should be further verified using
502 alternative geophysical methods, such as active seismics or electromagnetic methods. In case it is
503 approved, this would give a unique possibility to reach the magma storage by a relatively small
504 borehole and investigate it for the purposes of using the heat of active magma to produce
505 geothermal energy.

506

507 **Acknowledgments:**

508 We thank Jim Dixon from AVO who provided us the data for this study. IK was supported by
509 the Russian Science Foundation Grant # 20-17-00075.

510 Derived products from this publication, including travel times of P and S waves and the full
511 folder of the LOTOS code that allows reproducing all the results of this research are presented in
512 the file repository: Ekaterina Kasatkina, & Ivan Koulakov. (2022). Data and program codes to
513 reproduce the results of seismic tomography for Okmok [Data set]. Zenodo.
514 https://doi.org/10.5281/zenodo.6475984.

515 **Figure captions:**

516 **Figure 1.** Shaded-relief map of the Okmok volcano (Umnak Island, Alaska) and its location
517 within the Aleutian volcanic arc. Main eruptive features in the caldera shown sketchily after
518 Larsen et al. (2015) and represent the recent 2008 eruption formations – new tephra cone with
519 additional vents, area of collapsing pits and two renewed Cone D lakes. Post-caldera cones
520 marked by letters after Byers, 1959. Base map topography and bathymetry data was loaded from
521 www.marine-geo.org (GRMT data, Ryan et al., 2009); central part of the map (including
522 caldera) have been constructed with detailed DEM data from Schaefer et al, 2012. See features
523 descriptions in the legend.

Figure 2. Seismic network on the Okmok volcano and spatial seismicity distribution used for tomographic inversion in this study. Seismic events (2003 – 2017) are shown by dots colored by focal depth. Purple and lilac triangles depict two types of seismic instruments with its ID's. Gray star indicate Ranch house at Fort Glenn Cape field.

Figure 3. Results of the checkerboard test for determining horizontal resolution. Results of recovery are presented for P -, S - and Vp/Vs models at 4 and 7 km depth levels. Initial configuration of synthetic 5-km-side anomalies with 1 km intervals is highlighted with the dotted lines. The thin black lines shows topography contours with 200 m intervals.

Figure 4. Results of three checkerboard tests for checking the vertical resolution in which the synthetic models were defined along three vertical sections, same as indicated in Figure 8. The recovery results are presented for the Vp and Vs anomalies and Vp/Vs ratio. The shapes of the synthetic anomalies are highlighted with the dotted lines.

Figure 5. Synthetic tests for checking the resolution in the deeper part of the model. The synthetic models were defined along three vertical sections, same as indicated in Figure 8. The recovery results are presented for the Vp and Vs anomalies and Vp/Vs ratio. The shapes of the synthetic anomalies are highlighted with the dotted lines.

Figure 6. Results of recovery of two synthetic models with realistic shapes of anomalies defined along Section 1 (same as used for presenting the main results in Figure 8). The initial synthetic patterns are shown in the upper row; the values of the P and S wave velocity anomalies are indicated by two numbers inside each pattern. The results of the recovery are shown for the Vp/Vs ratio in the lower row. The shapes of the initial anomalies are highlighted with the dotted lines. The comparison of the results of these two tests gives a possibility to assess the reliability of the deep conduit resolving.

Figure 7. Mislocations of the sources during the synthetic modeling (for the model indicated in the right column in Figure 6) shown in the map view and vertical section. Upper row is the location results with the use of the starting 1D model, and the lower row is the location results in the final 3D velocity model. Black dots indicate the current locations of events, and the red bars direct to the true locations. The mean errors of source locations are indicated in figure captions.

Figure 8. The distributions of the resulting anomalies of Vp, Vs and Vp/Vs ratio in four horizontal sections. The red dots indicate the locations of seismic events at the vicinity of the

corresponding depth levels. The thin black lines shows topography contours with 200 m intervals.

Figure 9. The distributions of the resulting anomalies of Vp, Vs and Vp/Vs ratio in three vertical sections with the locations shown in Figure 7. The black dots indicate the projections of seismic events located at distances of less than 2 km from the profile. The numbered dotted lines indicate the intersections with other sections.

Figure 10. Schematic interpretation of the resulting distributions of the Vp/Vs ratio in sections 1 and 3 in terms of conduits (filled red zones) and magma reservoirs (empty red contours). The yellow dots indicate the seismicity along the sections. On the surface, the detailed topography with the locations of the 1817, 1997 and 2008 eruptions is shown. More details with the description of this figure are in the Discussion section.

References:

Bennington, N. L., Haney, M., De Angelis, S., Thurber, C. H., and Freymueller J. (2015). Monitoring changes in seismic velocity related to an ongoing rapid inflation event at Okmok volcano, Alaska, *Journal of Geophysical Research: Solid Earth*, 120, 5664–5676, https://doi.org/10.1002/2015JB011939

Bennington, N. L., Ohlendorf, S. J., Thurber, C. H., & Haney, M. M. (2021). Spatiotemporal analysis of seismic velocity changes at Okmok volcano, Alaska and implications from deformation source modeling. *Earth and Planetary Science Letters*, *561*, 116809

Biggs, J., Lu, Z., Fournier, T., & Freymueller, J. T. (2010). Magma flux at Okmok Volcano, Alaska, from a joint inversion of continuous GPS, campaign GPS, and interferometric synthetic aperture radar. *Journal of Geophysical Research: Solid Earth*, 115 (B12), https://doi.org/10.1029/2010JB007577

Bushenkova, N., Koulakov, I., Senyukov, S., Gordeev, E.I., Huang, H.-H., El Khrepy, S. & Al Arifi, N. (2019). Tomographic images of magma chambers beneath the Avacha and Koryaksky volcanoes in Kamchatka. *Journal of Geophysical Research: Solid Earth*, 124, 9694-9713, https://doi.org/10.1029/2019JB017952

584 Dixon, J. P., Cameron, C. E., Iezzi, A. M. & Wallace, K. (2017). 2015 Volcanic activity in
585 Alaska-Summary of events and response of the Alaska Volcano Observatory. *U.S.*
586 *Geological Survey Scientific Investigations Report*, 2017-5104, 61,
587 https://doi.org/10.3133/sir20175104

588 Haney, M.M. (2010). Location and mechanism of very long period tremor during the 2008
589 eruption of Okmok Volcano from interstation arrival times, *Journal of Geophysical*
590 *Research*, 115, 13, https://doi.org/10.1029/2010JB007440

591 Finney, B., Turner, S., Hawkesworth, C., Larsen, J., Nye, C., George, R. et al. (2008).
592 Magmatic Differentiation at an Island-arc Caldera: Okmok Volcano, Aleutian
593 Islands, Alaska. *Journal of Petrology*, 49 (5), 857–884,
594 https://doi.org/10.1093/petrology/egn008

595 Fournier, T., Freymueller, J., & Cervelli, P. (2009). Tracking magma volume recovery at
596 Okmok volcano using GPS and an unscented Kalman filter. *Journal of Geophysical*
597 *Research*, 114, B02405, https://doi.org/10.1029/2008JB005837

598 Freymueller, J.T., Kaufman, A.M. (2010). Changes in the magma system during the 2008
599 eruption of Okmok volcano, Alaska, based on GPS measurements. *Journal of*
600 *Geophysical Research*, 115 (B12), https://doi.org/10.1016/j.jvolgeores.2012.04.021

601 Guffanti, M., Casadevall, T.J., & Budding, K. (2010). Encounters of aircraft with volcanic
602 ash clouds: A compilation of known incidents, 1953–2009. *U.S. Geological Survey*
603 *Data Series*, 545, 1.0, 12

604 Haney, M. M. (2010). Location and mechanism of very long period tremor during the 2008
605 eruption of Okmok Volcano from interstation arrival times. *Journal of Geophysical*
606 *Research: Solid Earth*, 115, B00B05, https://doi.org/10.1029/2010JB007440

607 Johnson, J. H., Prejean, S., Savage, M. K., & Townend, J. (2010). Anisotropy, repeating
608 earthquakes, and seismicity associated with the 2008 eruption of Okmok volcano,
609 Alaska. *Journal of Geophysical Research: Solid Earth*, 115, B00B04,
610 https://doi.org/10.1029/2009JB006991

611 Kasatkina, E., Koulakov, I., West, M., & Izbekov, P. (2014). Seismic structure changes
612 beneath Redoubt Volcano during the 2009 eruption inferred from local earthquake
613 tomography. *Journal of Geophysical Research: Solid Earth*, 119, 4938–4954,
614 https://doi.org/10.1002/2013JB010935

615 Koulakov, I. (2009). LOTOS code for local earthquake tomographic inversion:
616 Benchmarks for testing tomographic algorithms. *Bulletin of the Seismological*
617 *Society of America*, 99, 194–214, https://doi.org/10.1785/0120080013

618 Koulakov I., Abkadyrov, I., Al Arifi, N., Deev, E., Droznina, S., Gordeev E. I. et al.
619 (2017). Three different types of plumbing system beneath the neighboring active
620 volcanoes of Tolbachik, Bezymianny, and Klyuchevskoy in Kamchatka. *Journal of*
621 *Geophysical Research: Solid Earth*, 122, https://doi.org/10.1002/2017JB014082.

622 Koulakov I., Boychenko E. & Smirnov, S.Z. (2020). Magma chambers and meteoric fluid
623 flows beneath the Atka volcanic complex (Aleutian Islands) inferred from local
624 earthquake tomography. *Geosciences*, 10, 214,
625 https://doi.org/10.3390/geosciences10060214.

626 Koulakov, I., Kasatkina, E., Shapiro, N. M., Jaupart, C., Vasilevsky, A., El Khrepy, S. et
627 al. (2016). The feeder system of the Toba supervolcano from the slab to the shallow
628 reservoir, *Nature Communications*. 7:12228, https://doi.org/10.5194/se-7-965-2016.

629 Koulakov, I., Komzeleva, V, Smirnov, S.Z. & Bortnikova S.B. (2021). Magma-fluid
630 interactions beneath Akutan Volcano in the Aleutian Arc based on the results of local
631 earthquake tomography. *Journal of Geophysical Research: Solid Earth*, 126 (1),
632 e2020JB021192, https://doi.org/10.1029/2020JB021192.

633 Koulakov, I., West, M., & Izbekov, P. (2013). Fluid ascent during the 2004–2005 unrest at
634 Mt. Spurr inferred from seismic tomography. *Geophysical Research Letters*, 40 (17),
635 4579–4582, https://doi.org/10.1002 /grl.50674.

636 Larsen, J. F., Neal, C., Schaefer, J., Beget, J., & Nye, C. (2007). Late Pleistocene and
637 Holocene caldera-forming eruptions of Okmok caldera, Aleutian islands, Alaska.
638 *Washington DC American Geophysical Union Geophysical Monograph Series*, *172*,
639 343-364, https://doi.org/10.1029/172GM24

640 Larsen, J. F., Neal, C., Webley, P., Freymueller, J., Haney, M., McNutt, S., & Wessels, R.
641 (2009). Eruption of Alaska volcano breaks historic pattern. *Eos: Transactions*
642 *American Geophysical Union*, *90*(20), 173-174

643 Larsen, J. F., Schaefer, C. A., Kaufman, J. R., & Lu, Z. (2015). The 2008 phreatomagmatic
644 eruption of Okmok Volcano, Aleutian Islands, Alaska: Chronology, deposits, and
645 landform changes. *Bulletin of Volcanology*, 77 (69), https://doi.org/10.1007/s00445-
646 015-0952-9

Larsen, J. F., Śliwiński, M. G., Nye, C., Cameron, C., & Schaefer, J. R. (2013). The 2008 eruption of Okmok Volcano, Alaska: Petrological and geochemical constraints on the subsurface magma plumbing system. *Journal of Volcanology and Geothermal Research*, *264*, 85-106, https://doi.org/10.1016/j.jvolgeores.2013.07.003

Mann, D., Freymueller, J., & Lu, Z. (2002). Deformation associated with the 1997 eruption of Okmok volcano, Alaska. *Journal of Geophysical Research: Solid Earth*, 107(B4), 2072, https://doi.org/10.1029/2001JB000163

Masterlark, T., Haney, M., Dickinson, H., Fournier, T., & Searcy, C. (2010). Rheologic and structural controls on the deformation of Okmok volcano, Alaska: FEMs, InSAR, and ambient noise tomography. *Journal of Geophysical Research: Solid Earth*, *115*(B2), B02409, https://doi.org/10.1029/2009JB006324

Masterlark, T., Feigl K. L., Haney M., Stone J., Thurber C., & Ronchin E. (2012). Nonlinear estimation of geometric parameters in FEMs of volcano deformation: Integrating tomography models and geodetic data for Okmok volcano, Alaska. *Journal of Geophysical Research*, 117, B02407, https://doi.org/10.1029/2011JB008811

McConnell, J. R., Sigl, M., Plunkett, G., Burke, A., Kim, W. M., Raible, C.C. et al. (2020). Extreme climate after massive eruption of Alaska's Okmok volcano in 43 BCE and effects on the late Roman Republic and Ptolemaic Kingdom. *Proceedings of the National Academy of Sciences*. 117 (27): 15443–5449, https://doi.org/10.1073/pnas.2002722117

Miller, T.P., McGimsey, R.G., Richter, D.H., Riehle, J.R., Nye, C.J., Yount, M.E. & Dumoulin, J.A. (1998). Catalog of the historically active volcanoes of Alaska. *Department of the Interior, U.S. Geological Survey*, 98–582 (104).

Nolet, G. (1987). Seismic wave propagation and seismic tomography. *Seismic Tomography*, 1–23, https://doi.org/10.1007/978-94-009-3899-1_1

Nye, C. J., Motyka, R. J., Turner, D. L., & Liss, S. A. (1990). Geology and geochemistry of the Geyser Bight Geothermal Area, Umnak Island, Aleutian Islands, Alaska. Fairbanks, AK: *Graphic North Printing, Division of Geological and Geophysical Surveys*

Ohlendorf, S. J., Thurber, C. H., Pesicek, J. D., & Prejean, S. G. (2014). Seismicity and seismic structure at Okmok Volcano, Alaska. *Journal of Volcanology and*

679 *Geothermal Research*, *278*, 103-119,
680 https://doi.org/10.1016/j.jvolgeores.2014.04.002

681 Paige, C.C., & Saunders, M.A. (1982). LSQR: An algorithm for sparse linear equations
682 and sparse least squares. *ACM Transactions on Mathematical Software*, 8(1), 43–71,
683 https://doi.org/10.1145/355984.355989

684 Pesicek, J. D., Sileny, J., Prejean, S. G., & Thurber, C. H. (2012). Determination and
685 uncertainty of moment tensors for microearthquakes at Okmok Volcano, Alaska.
686 *Geophysical Journal International*, 190(3), 1689-1709,
687 https://doi.org/10.1111/j.1365-246X.2012.05574.x

688 Qu, F., Lu, Z., Poland, M., Freymueller, J., Zhang, Q., & Jung, H. S. (2015). Post-eruptive
689 inflation of Okmok volcano, Alaska, from InSAR, 2008–2014. *Remote Sensing*,
690 7(12), 16778-16794, https://doi.org/10.3390/rs71215839

691 Ryan, W.B.F., Carbotte S.M., Coplan J.O., O'Hara S., Melkonian A., Arko R. et al. (2009).
692 Global Multi-Resolution Topography synthesis. *Geochemistry, Geophysics,*
693 *Geosystems*, 10, Q03014, https://doi.org/10.1029/2008GC002332

694 Schaefer, J.R., Larsen, J.F., and Unema, J.A. (2012). Digital elevation model (DEM) and
695 shaded relief image of Okmok Caldera, 2010. *Alaska Division of Geological &*
696 *Geophysical Surveys* Raw Data File 2011-6, http://doi.org/10.14509/23223

697 Takei, Y. (2002). Effect of pore geometry on VP/VS: From equilibrium geometry to crack.
698 *Journal of Geophysical Research*, 107, 2043, https://doi.org/10.1029/2001JB000522

699 Um, J., & Thurber, C.H. (1987). A fast algorithm for two-point seismic ray tracing.
700 *Bulletin of the Seismological Society of America*, 77, 972–986.

701 Walwer, D., Ghil, M., & Calais, E. (2019). Oscillatory nature of the Okmok volcano's
702 deformation. *Earth and Planetary Science Letters*, 506, 76–86,
703 https://doi.org/10.1016/j.epsl.2018.10.033

704 Xue, X., Freymueller, J., & Lu, Z. (2020). Modeling the posteruptive deformation at
705 Okmok based on the GPS and InSAR time series: Changes in the shallow magma
706 storage system. *Journal of Geophysical Research: Solid Earth*, 125, e2019JB017801.
707 https://doi.org/10.1029/2019JB017801

708 Yaroshenko, G., Koulakov, I., Al-Arifi, N., Qaysi S., & El-Khrepy, S. (2022). Structure of
709 the magma plumbing system beneath Semisopochnoi Island (Aleutian Arc) inferred
710 from seismic tomography. *Scientific Reports* (in press)

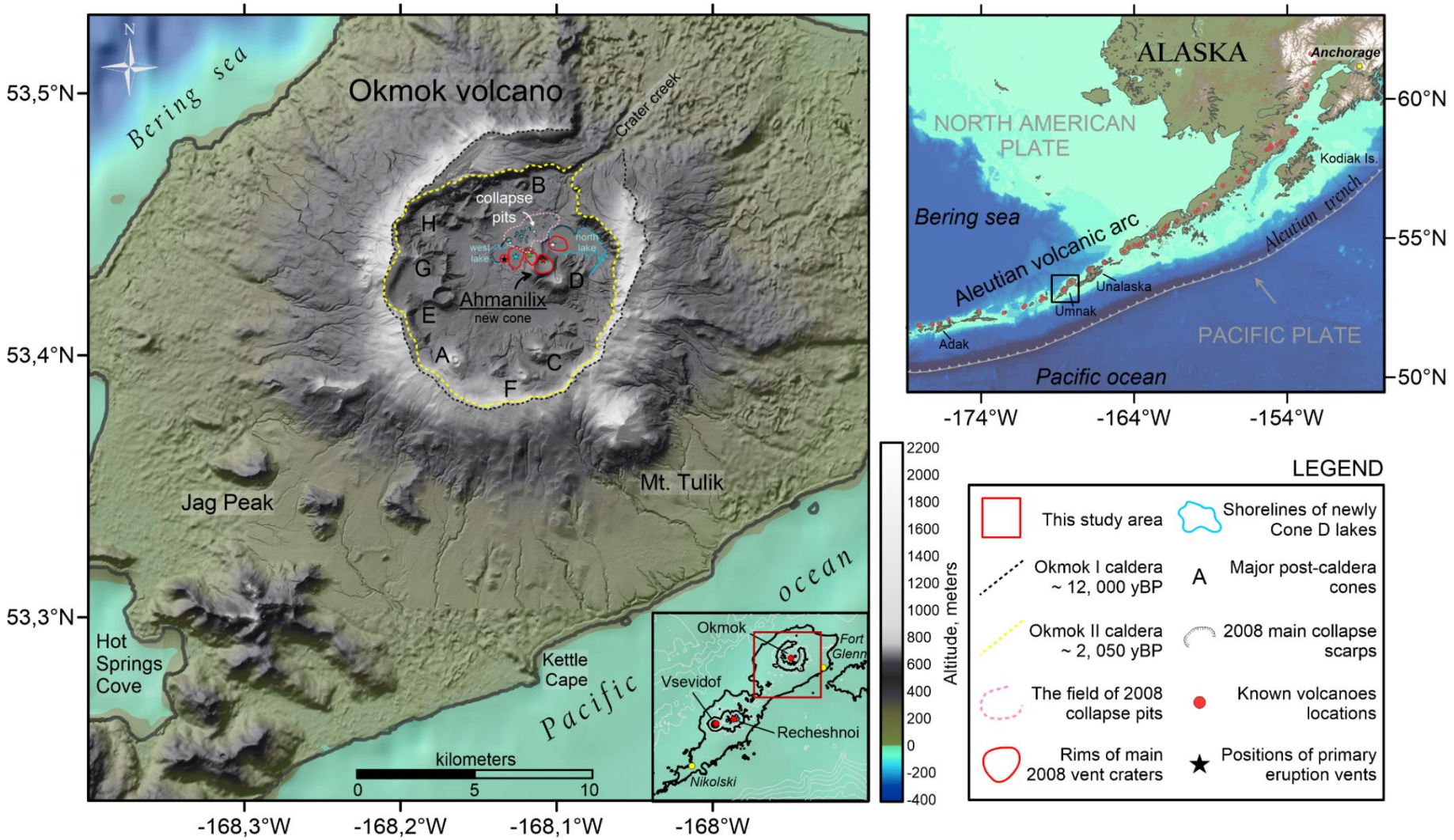

Figure 1. Shaded-relief map of the Okmok volcano (Umnak Island, Alaska) and its location within the Aleutian volcanic arc. Main eruptive features in the caldera shown sketchily after Larsen et al. (2015) and represent the recent 2008 eruption formations – new tephra cone with additional vents, area of collapsing pits and two renewed Cone D lakes. Post-caldera cones marked by letters after Byers, 1959. Base map topography and bathymetry data was loaded from www.marine-geo.org (GRMT data, Ryan et al., 2009); central part of the map (including caldera) have been constructed with detailed DEM data from Schaefer et al, 2012. See features descriptions in the legend.

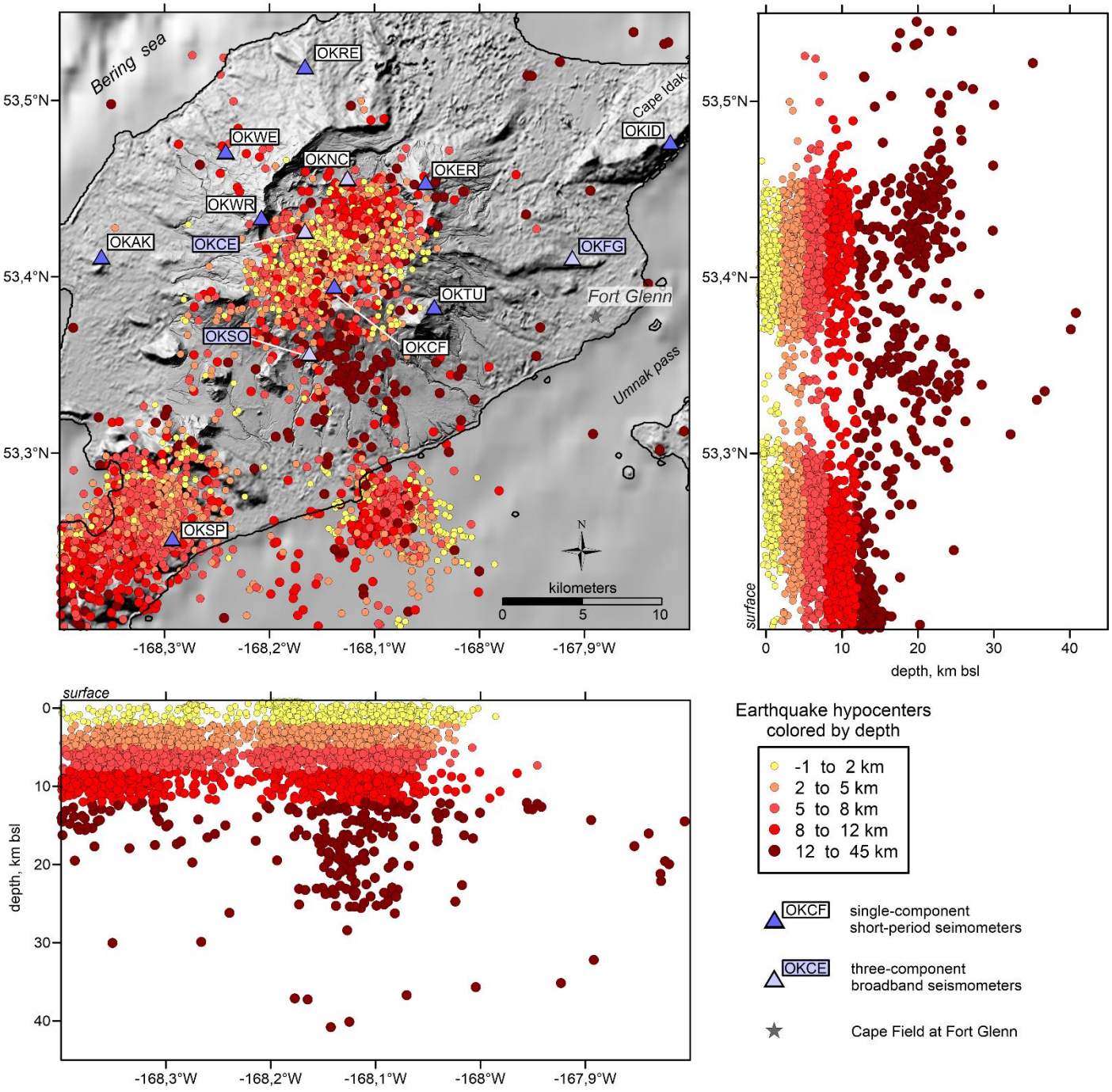

Figure 2. Seismic network on the Okmok volcano and spatial seismicity distribution used for tomographic inversion in this study. Seismic events (2003 – 2017) are shown by dots colored by focal depth. Purple and lilac triangles depict two types of seismic instruments with its ID's. Gray star indicate Ranch house at Fort Glenn Cape field.

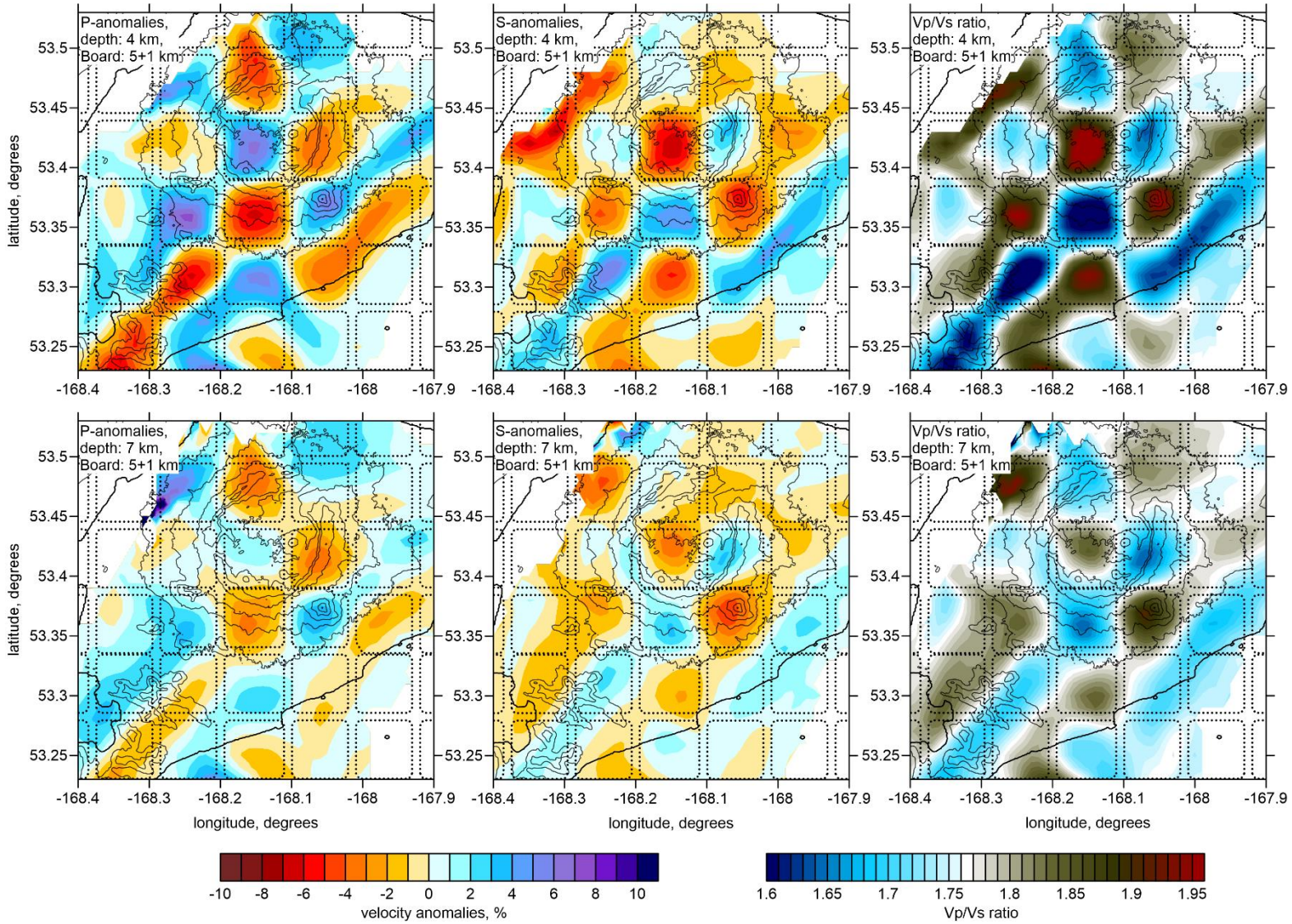

Figure 3. Results of the checkerboard test for determining horizontal resolution. Results of recovery are presented for P -, S - and Vp/Vs models at 4 and 7 km depth levels. Initial configuration of synthetic 5-km-side anomalies with 1 km intervals is highlighted with the dotted lines. The thin black lines shows topography contours with 200 m intervals.

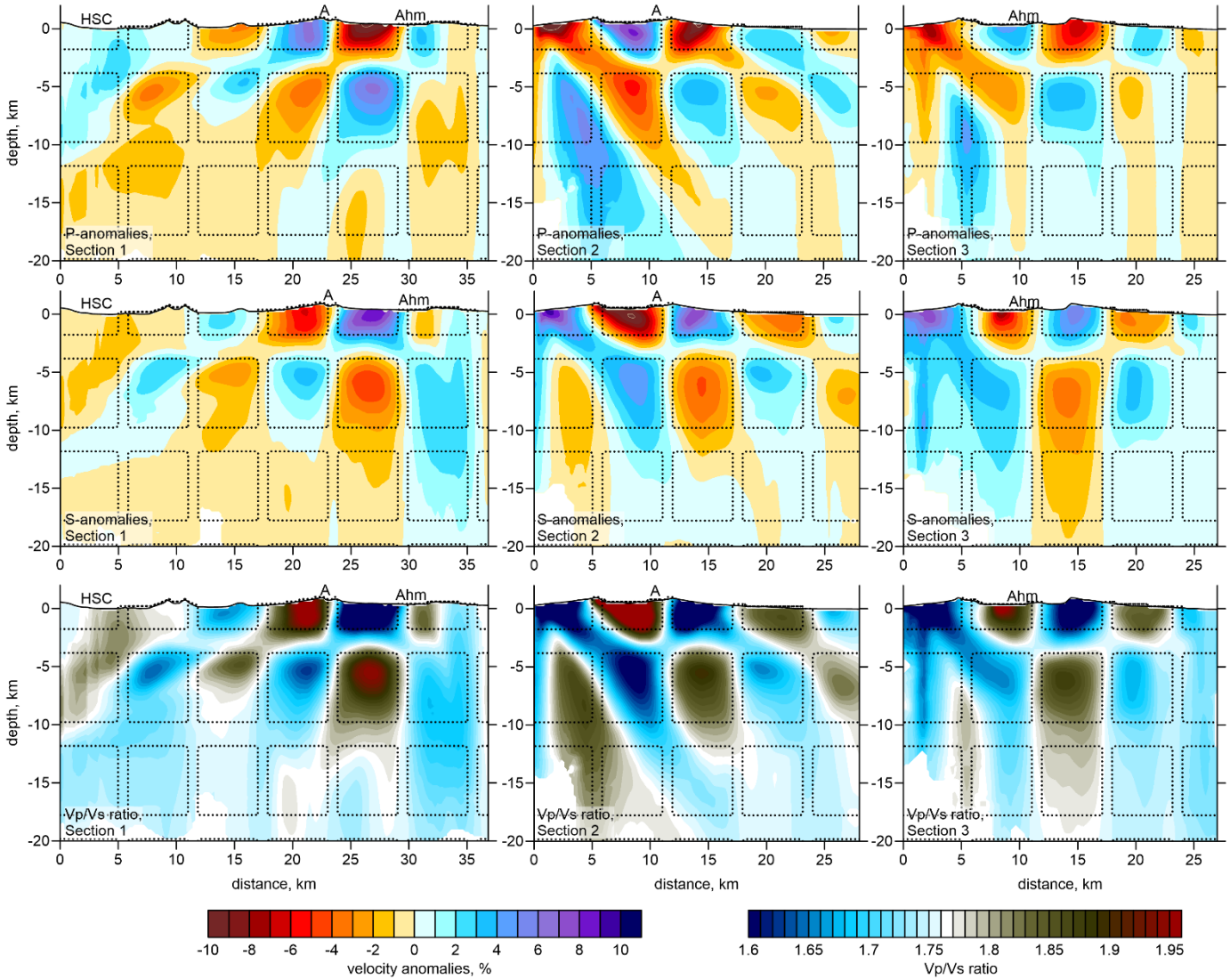

Figure 4. Results of three checkerboard tests for checking the vertical resolution in which the synthetic models were defined along three vertical sections, same as indicated in Figure 8. The recovery results are presented for the Vp and Vs anomalies and Vp/Vs ratio. The shapes of the synthetic anomalies are highlighted with the dotted lines.

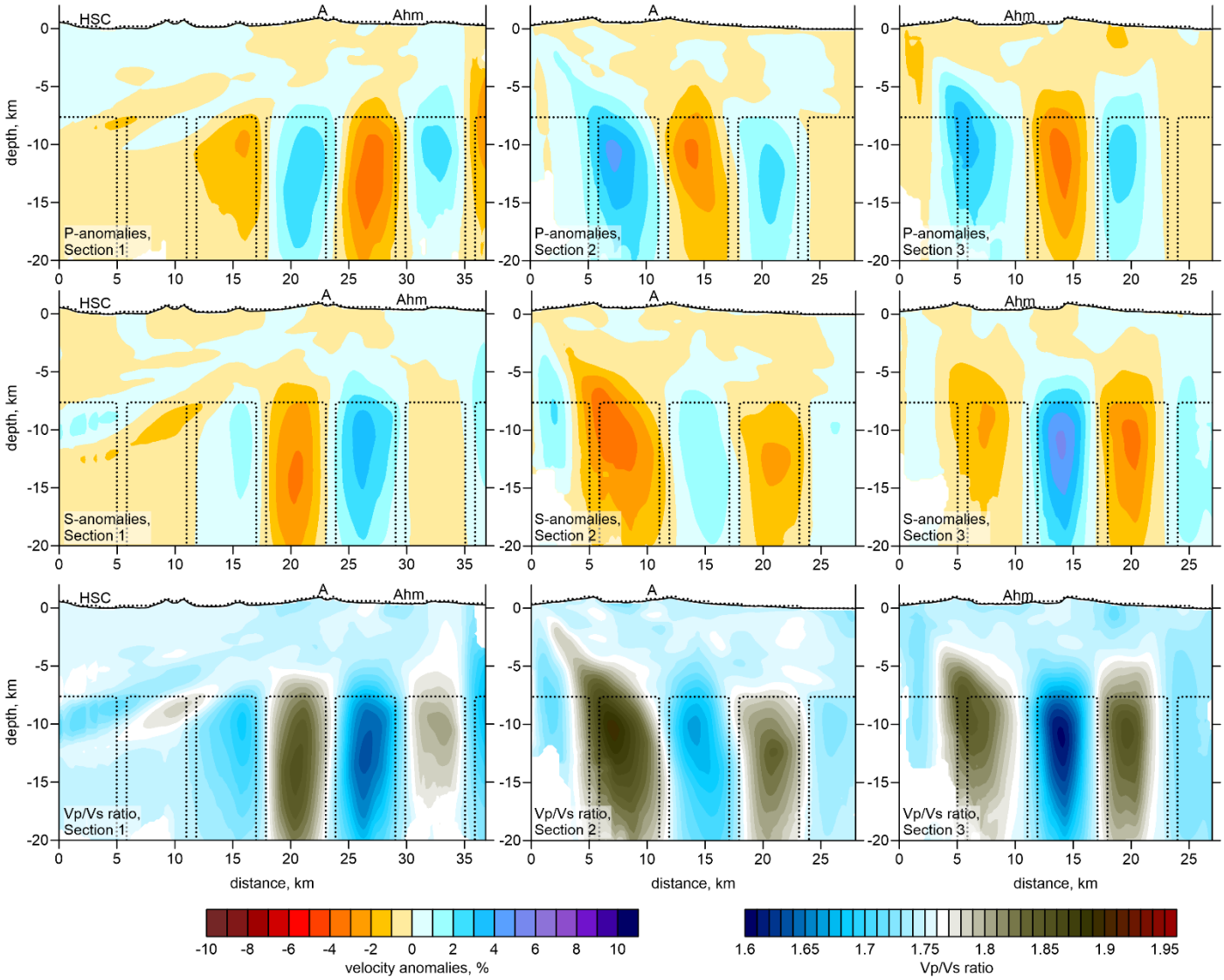

Figure 5. Synthetic tests for checking the resolution in the deeper part of the model. The synthetic models were defined along three vertical sections, same as indicated in Figure 8. The recovery results are presented for the Vp and Vs anomalies and Vp/Vs ratio. The shapes of the synthetic anomalies are highlighted with the dotted lines.

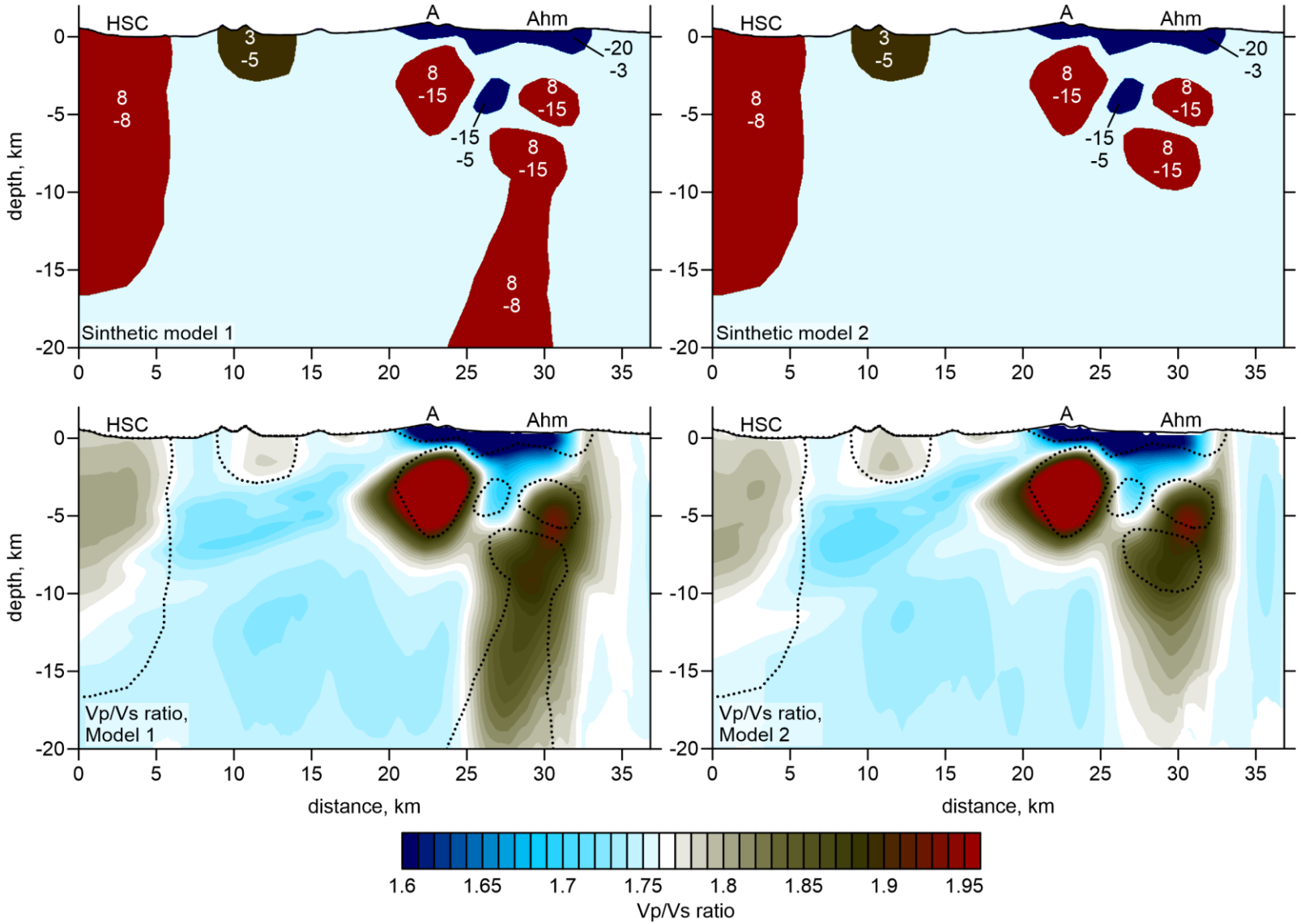

Figure 6. Results of recovery of two synthetic models with realistic shapes of anomalies defined along Section 1 (same as used for presenting the main results in Figure 8). The initial synthetic patterns are shown in the upper row; the values of the P and S wave velocity anomalies are indicated by two numbers inside each pattern. The results of the recovery are shown for the Vp/Vs ratio in the lower row. The shapes of the initial anomalies are highlighted with the dotted lines. The comparison of the results of these two tests gives a possibility to assess the reliability of the deep conduit resolving.

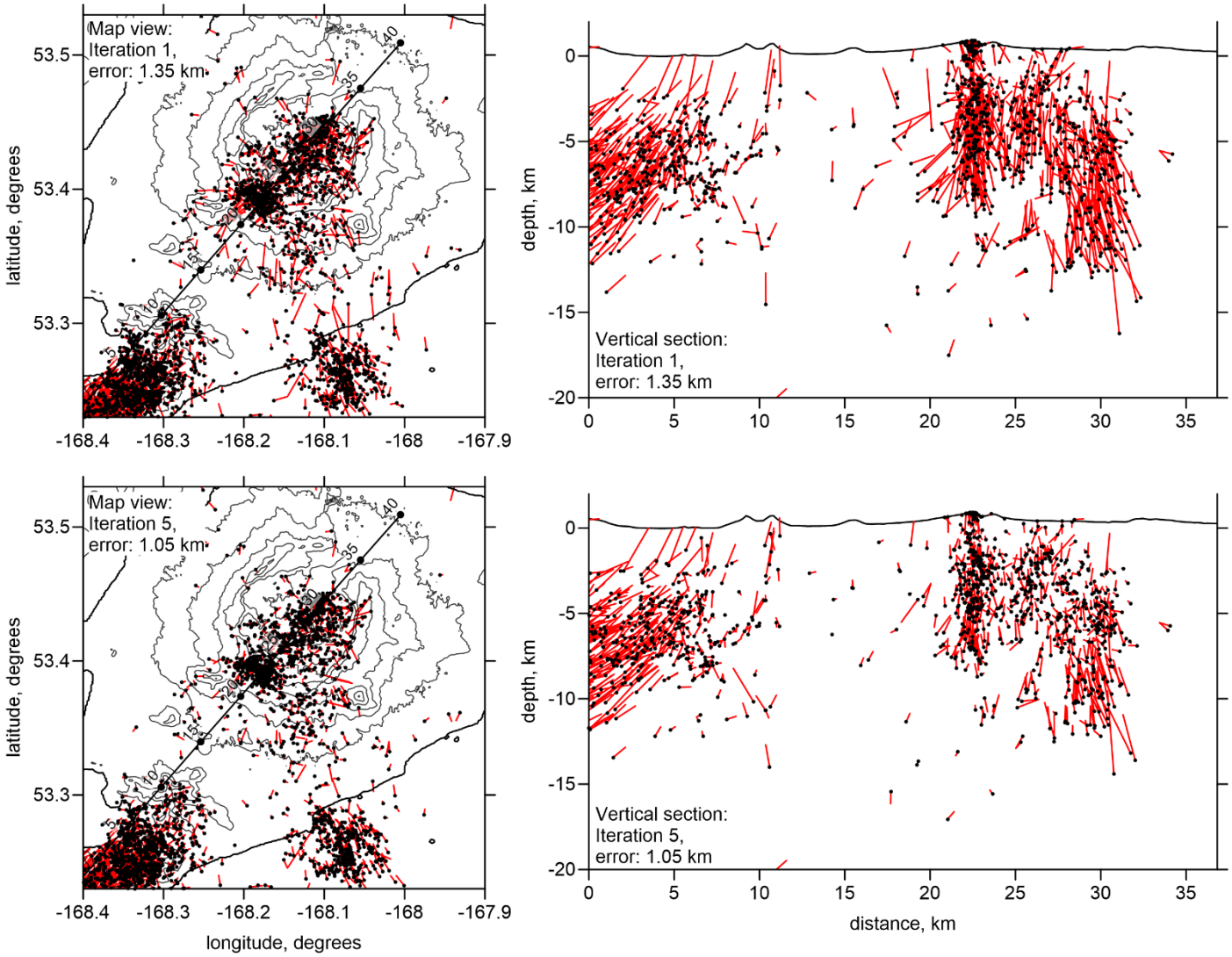

Figure 7. Mislocations of the sources during the synthetic modeling (for the model indicated in the right column in Figure 6) shown in the map view and vertical section. Upper row is the location results with the use of the starting 1D model, and the lower row is the location results in the final 3D velocity model. Black dots indicate the current locations of events, and the red bars direct to the true locations. The mean errors of source locations are indicated in figure captions.

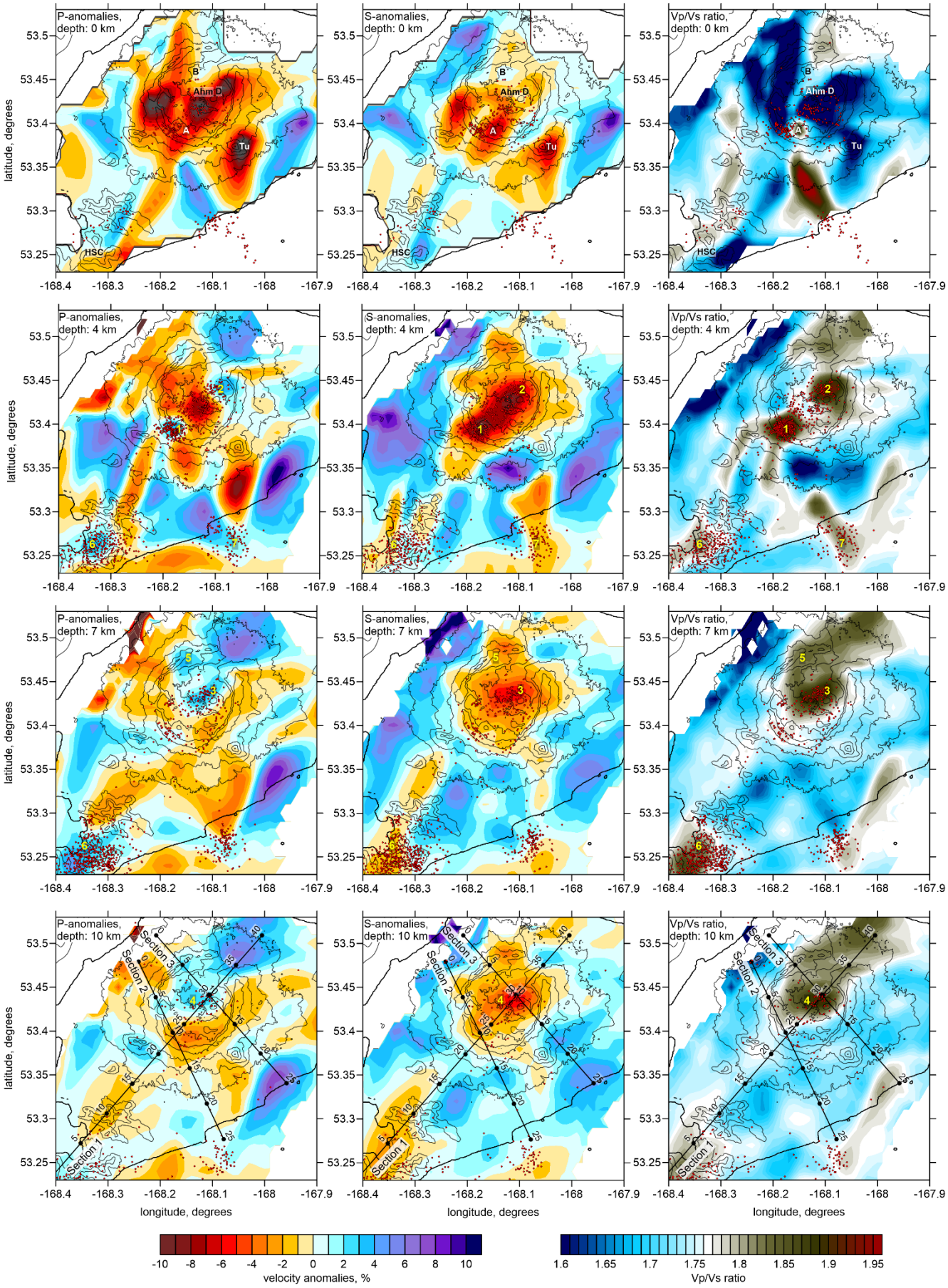

Figure 8. The distributions of the resulting anomalies of Vp, Vs and Vp/Vs ratio in four horizontal sections. The red dots indicate the locations of seismic events at the vicinity of the corresponding depth levels. The thin black lines shows topography contours with 200 m intervals.

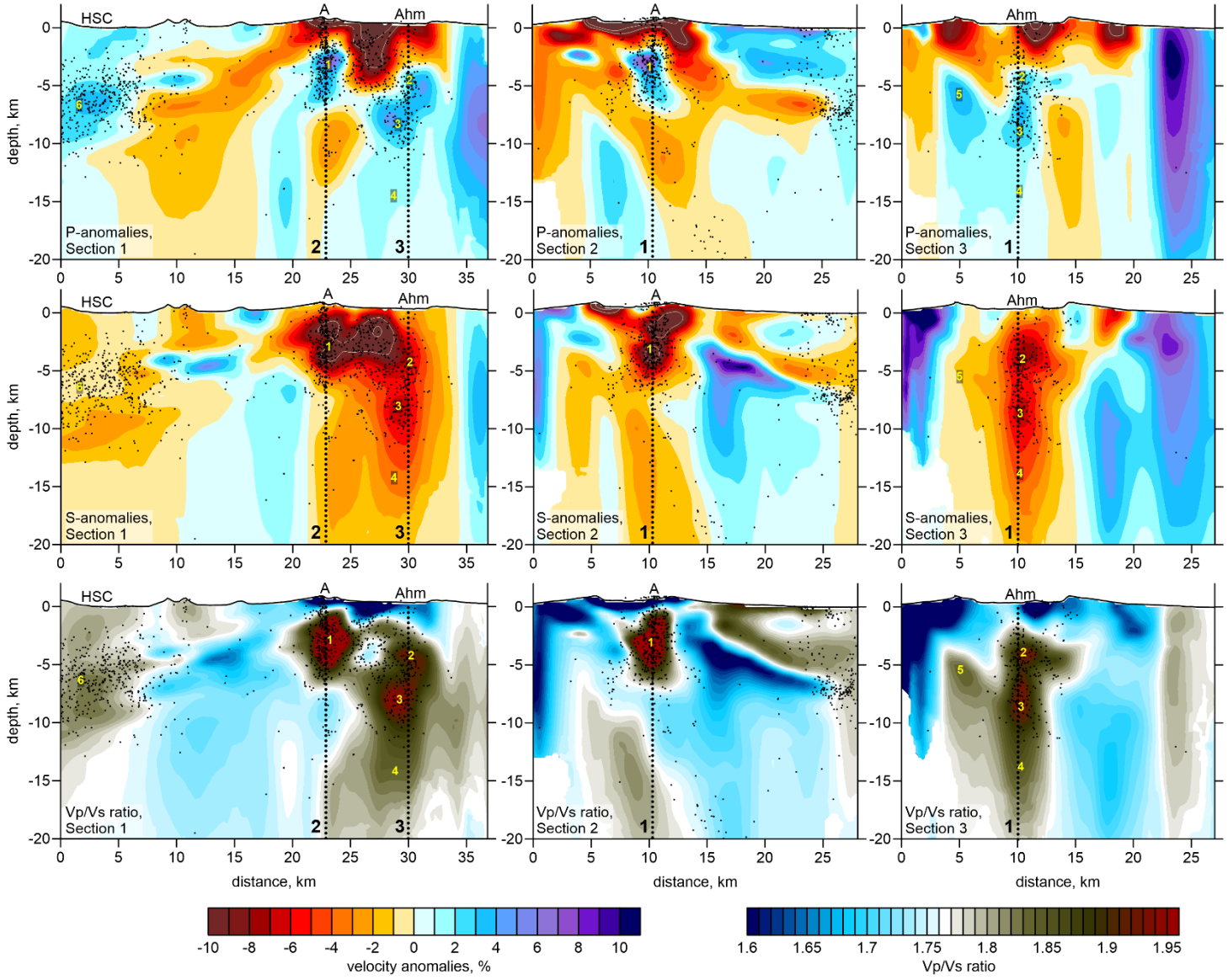

Figure 9. The distributions of the resulting anomalies of Vp, Vs and Vp/Vs ratio in three vertical sections with the locations shown in Figure 7. The black dots indicate the projections of seismic events located at distances of less than 2 km from the profile. The numbered dotted lines indicate the intersections with other sections.

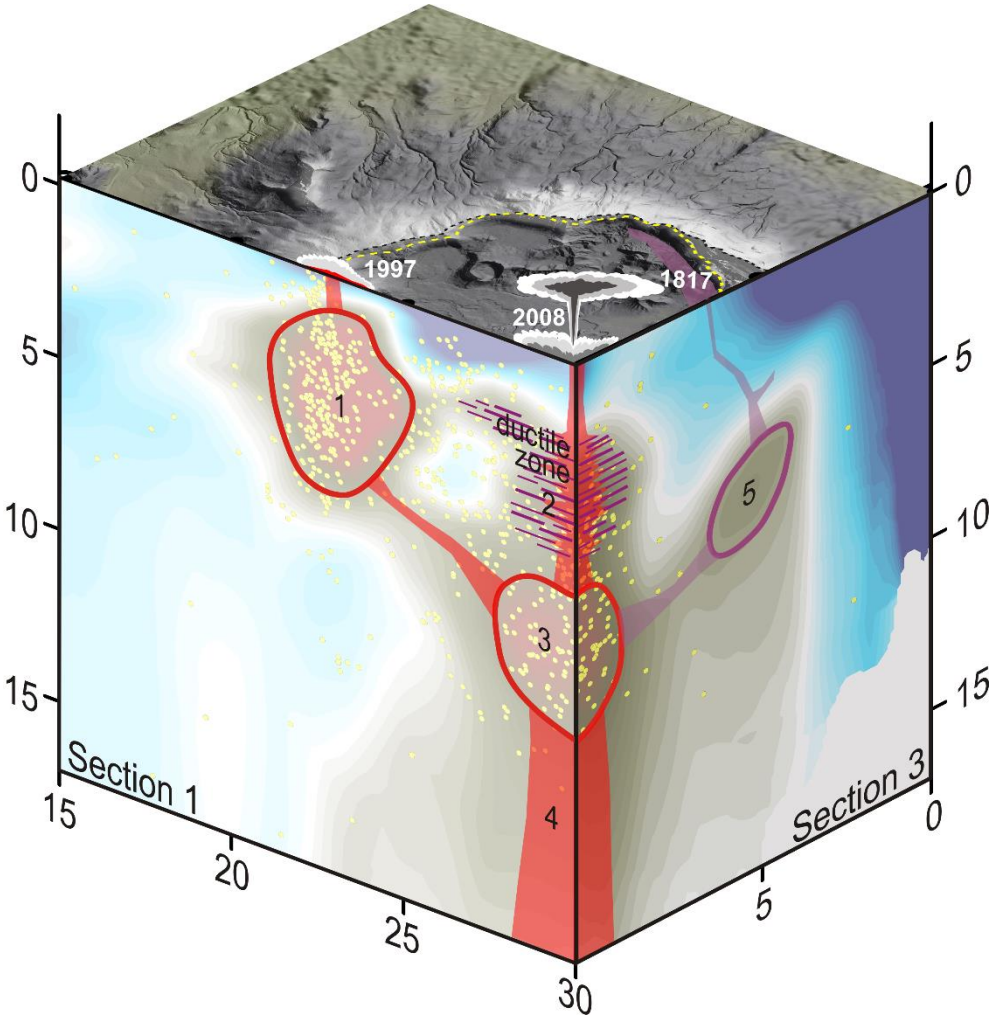

Figure 10. Schematic interpretation of the resulting distributions of the Vp/Vs ratio in sections 1 and 3 in terms of conduits (filled red zones) and magma reservoirs (empty red contours). The yellow dots indicate the seismicity along the sections. On the surface, the detailed topography with the locations of the 1817, 1997 and 2008 eruptions is shown. More details with the description of this figure are in the Discussion section.